Aleksander Jaworski*, Jędrzej Piątek, Liuda Mereacre, Cordula Braun and Adam Slabon*

^{14}N, ^{13}C, and ^{119}Sn solid-state NMR characterization of tin(II) carbodiimide Sn(NCN)

https://doi.org/10.1515/znb-2021-0122
Received August 26, 2021; accepted September 2, 2021;
published online September 29, 2021

Abstract: We report the first magic-angle spinning (MAS) nuclear magnetic resonance (NMR) study on Sn(NCN). In this compound the spatially elongated $(NCN)^{2-}$ ion is assumed to develop two distinct forms: either cyanamide ($N{\equiv}C{-}N^{2-}$) or carbodiimide ($^{-}N{=}C{=}N^{-}$). Our ^{14}N MAS NMR results reveal that in Sn(NCN) the $(NCN)^{2-}$ groups exist exclusively in the form of symmetric carbodiimide ions with two equivalent nitrogen sites, which is in agreement with the X-ray diffraction data. The ^{14}N quadrupolar coupling constant $|C_Q| \approx 1.1$ MHz for the $^{-}N{=}C{=}N^{-}$ ion in Sn(NCN) is low when compared to those observed in molecular compounds that comprise cyano-type N≡C– moieties ($|C_Q| > 3.5$ MHz). This together with the information from ^{14}N and ^{13}C chemical shifts indicates that solid-state NMR is a powerful tool for providing atomic-level insights into anion species present in these compounds. The experimental NMR results are corroborated by high-level calculations with quantum chemistry methods.

Keywords: DLPNO-CCSD; DSD-PBEP86; ^{14}N MAS NMR; $SnCN_2$; ^{119}Sn MAS NMR.

Dedicated to: Professor Richard Dronskowski of the Rwth Aachen on the occasion of his 60th birthday.

1 Introduction

Metal carbodiimides $M_x(NCN)_y$ (where M = alkali, alkaline-earth, rare-earth, or transition metal) are a class of inorganic compounds originally derived from molecular cyanamide, $H_2N{-}C{\equiv}N$, or the unstable carbodiimide isomer, H–N=C=N–H [1, 2]. Furthermore, metal oxide carbodiimides as representatives of mixed-anion compounds can incorporate both types of anions to yield additional functionality [3–5]. Although Ca(NCN) has been known for a long time due to its application as nitrogen source for industry, it has been the last five years that carbodiimides have occurred as prospective materials for lighting and energy applications [6, 7]. The carbodiimides M(NCN) (M = Mn, Co) have been demonstrated as photoelectrodes for photoelectrochemical (PEC) water-splitting, whereas Ag_2(NCN) is one rare example of a cyanamide that is active for the oxygen evolution reaction (OER) and for the photochemical CO_2 reduction reaction [8–10]. Besides solar energy conversion, energy storage in carbodiimides has been reported by Dronskowski and coworkers in 2016 for several compounds M(NCN) (M = Mn, Fe, Zr, Cr) as electrode materials in both Na- and Li-ion batteries [11, 12]. Subsequent reports have disclosed synthetic approaches to obtain nanostructured carbodiimides and investigated size effects on the electrochemical storage capacity [13, 14].

Among the carbodiimides, Sn(NCN) can be considered as a versatile compound for materials science since (*i*) it can be doped with rare-earth elements to yield phosphors and (*ii*) favorable photochemical properties, as well as (*iii*) its application as electrode materials in Li-ion batteries [15]. Sn(NCN) can be reversible electrochemically lithiated according to following reaction:

$$Sn(NCN) + 2Li^{+} + 2e^{-} = Sn^{0} + Li_2(NCN) \quad (1)$$

During electrochemical cycling, it is most likely that several intermediate phases will be passed through. Within this respect, the advances in solid-state nuclear magnetic resonance (NMR) spectroscopy have helped to explore the chemistry of the electrode materials during charge and discharge of Li-ion batteries [16, 17].

Given the potential of Sn(NCN) as the electrode material in Li-ion batteries and the fact that there are no reports on solid-state NMR spectroscopic investigations to date for this class of compounds, in this study we provide atomic-level structural insights into Sn(NCN) with multinuclear ^{14}N, ^{13}C, and ^{119}Sn NMR spectroscopy. The experimental NMR parameters are confronted with the results obtained from accurate calculations with quantum chemistry methods.

***Corresponding authors: Aleksander Jaworski** and **Adam Slabon,** Department of Materials and Environmental Chemistry, Stockholm University, SE-106 91 Stockholm, Sweden,
E-mail: aleksander.jaworski@mmk.su.se (A. Jaworski); adam.slabon@mmk.su.se (A. Slabon)
Jędrzej Piątek, Department of Materials and Environmental Chemistry, Stockholm University, SE-106 91 Stockholm, Sweden
Liuda Mereacre and Cordula Braun, Institute for Applied Materials, Karlsruhe Institute of Technology, Herrmann-von-Helmholtz-Platz 1, 76344 Eggenstein-Leopoldshafen, Germany

2 Results and discussion

The graphical representation of the tin(II) carbodiimide Sn(NCN) crystal structure derived from X-ray diffraction [18, 19] is shown in Figure 1a. According to the diffraction data carbodiimide ($^{-}$N=C=N^{-}) ions in Sn(NCN) are symmetric and linear, and Sn^{2+} cations are four-coordinated in the distorted square pyramidal arrangement. The powder X-ray diffraction (PXRD) pattern of our Sn(NCN) sample (Figure 1b) was collected from the sample powder retrieved from the rotor after NMR experiments to exclude potential sample decomposition issues during magic-angle spinning (MAS). The PXRD data indicated minor amounts of $Sn_2O(NCN)$ and Sn_3N_4 impurity phases, similarly to previous reports on Sn(NCN) [15, 18].

In Figure 2a the ^{119}Sn MAS NMR spectrum of Sn(NCN) is presented. The spectrum reveals a broad pattern of spinning sidebands resulting from substantial chemical shift anisotropy (CSA) of the single Sn environment with an isotropic chemical shift δ_{iso} = −393 ppm, which is significantly lower than δ_{iso} = −208 ppm observed for SnO. This is consistent with the shielding effect induced by less electronegative nitrogen atoms, and therefore evidences more covalent bonding character in the carbodiimide compared to the oxide. The position of the isotropic signal was verified by performing experiments at different MAS rates and it was also checked with different offsets that the entire CSA pattern was excited. If we label the principal components of the NMR shift tensor (δ_{xx}, δ_{yy}, δ_{zz}; where $\delta_{iso} = (\delta_{xx} + \delta_{yy} + \delta_{zz})/3$) according to $|\delta_{zz} - \delta_{iso}| \geq |\delta_{xx} - \delta_{iso}| \geq |\delta_{yy} - \delta_{iso}|$ ("Haeberlen notation"), then the CSA can be expressed as $\delta_{aniso} = \delta_{zz} - \delta_{iso}$. The ^{119}Sn spectrum of Sn(NCN) indicates the $\delta_{aniso} \approx -600$ ppm, hence its magnitude is smaller than $\delta_{aniso} \approx -800$ ppm observed for SnO. However, the overall shape of the ^{119}Sn CSA pattern of Sn(NCN) exhibits close resemblance to that of SnO, which indicates that the local environment of the Sn^{2+} ion in the crystal structure of Sn(NCN) is similar to the square pyramidal (four-coordinated) arrangement in SnO, in agreement with the X-ray diffraction data [18]. The T_1 relaxation for the ^{119}Sn signal of Sn(NCN) was estimated to be ~12 s.

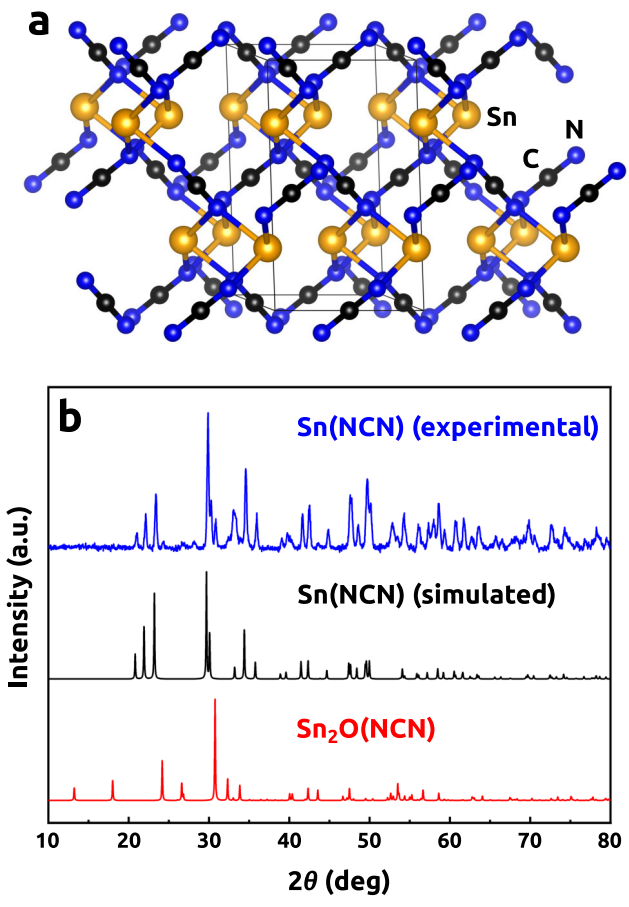

Figure 1: Crystal structure of the tin(II) carbodiimide Sn(NCN) with a unit cell indicated (a), and experimental XRPD pattern (b) collected from Sn(NCN) (blue trace). Crystallographic data from refs. [18, 19].

The small doublet centered at each sideband is visible close to the baseline in Figure 2a. This is attributed to the indirect $^1J(^{119}Sn–^{117}Sn)$ spin–spin couplings, which were also observed and analyzed by Amoureux and coworkers in the ^{119}Sn MAS NMR spectrum of SnO [20]. The splitting of ~2.2 kHz observed for Sn(NCN) is significantly smaller than ~8.3 kHz for SnO.

In Figure 2b the ^{13}C MAS NMR spectrum of Sn(NCN) is shown. The broad background signal centered at around 110 ppm originates from the polymer drive cap of the NMR rotor. The ^{13}C signal of the Sn(NCN) sample itself appears as a manifold of five sharp spinning sidebands that exhibit an isotropic chemical shift δ_{iso} = 148 ppm. This shift is slightly higher than those reported for dialkylcarbodiimides in the liquid state (136–143 ppm) [21, 22]. The ^{13}C CSA $\delta_{aniso} \approx -200$ ppm is large, as expected for the linear molecular geometry of the carbodiimide $^{-}$N=C=N^{-} ion. Noteworthy, the ^{13}C signal of Sn(NCN) exhibits very slow relaxation, and could only be recorded if a pulse delay of 3600 s was employed. This suggests the absence of molecular motion/dynamics in the crystal structure.

Despite 99.6% natural abundance of the ^{14}N isotope, the ^{15}N nucleus is the preferred one for solid-state NMR studies of nitrogen-containing materials. This is due to the spin I = 1and a considerable nuclear quadrupole moment of ^{14}N, which (in contrast to ^{15}N; I = 1/2) result in signals that are severely broadened by the quadrupolar interaction (proportionally to $3|C_Q|/2$, where $C_Q$is the ^{14}N quadrupolar

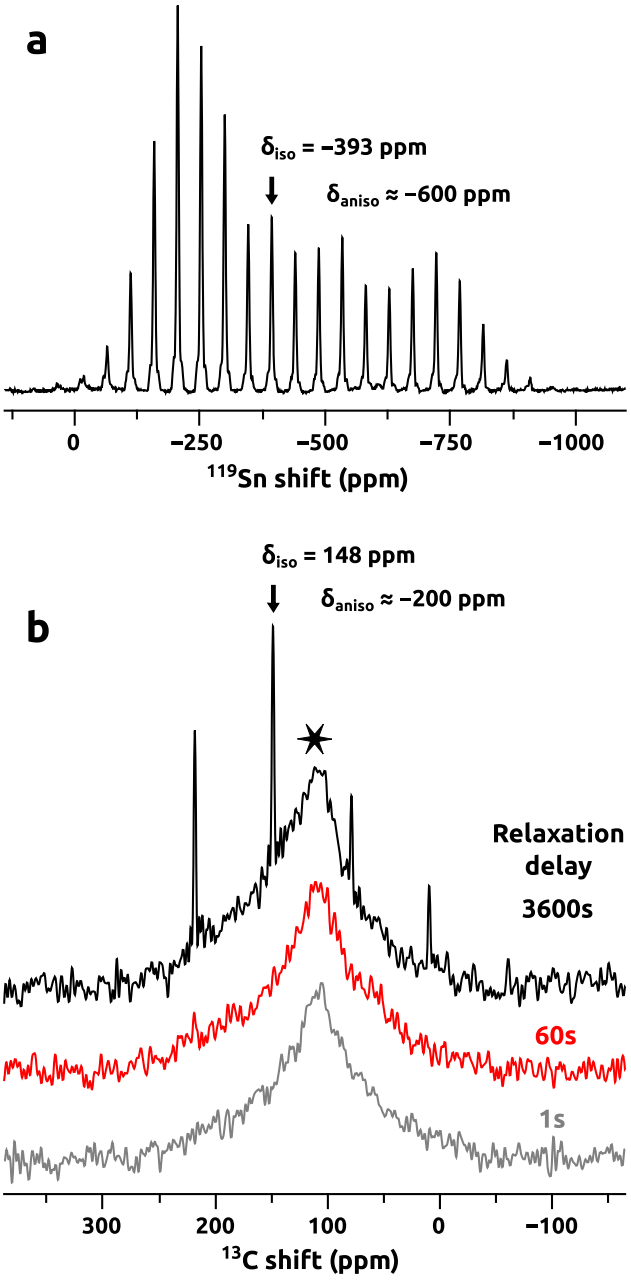

Figure 2: ^{119}Sn (panel a) and ^{13}C (panel b) MAS NMR spectra of Sn(NCN). The star in panel b denotes the background signal from polymer of the rotor cap.

coupling constant). With less than 0.4% natural abundance of ^{15}N isotope its direct NMR detection without isotope enrichment is challenging, although it has been shown to be feasible even with much lower nitrogen content in the material [23, 24]. However, we did not succeed to obtain ^{15}N NMR signal from Sn(NCN), which we attribute to very slow relaxation that is expected to be even slower than that of carbon, and accompanied by inherently lower sensitivity of ^{15}N compared to ^{13}C as a consequence of lower natural abundance and detection frequency. Instead, we focused on the detection and interpretation of the ^{14}N spectrum.

In Figure 3a the step-wise, variable-offset ^{14}N MAS NMR acquisition is presented. The gray pattern of spinning sidebands corresponds to the sum of all recorded subspectra and reflects the extent of the ^{14}N quadrupolar interaction in Sn(NCN). Its total width of around 1.6 MHz indicates rather low ^{14}N quadrupolar coupling constant $|C_Q| \approx 1.1$ MHz (note that the sign of the coupling is not discernible from the NMR spectrum). This is much lower than expected for cyano-type moieties (N≡C–). For example, ^{14}N quadrupolar coupling constants (estimated with rotational spectroscopy) for the acetonitrile molecule ($CH_3C^{14}N$) and for the terminal nitrogen atom in isocyanogen ($CNC^{14}N$) are –4.23 and –3.78 MHz, respectively [25, 26]. However, for the "inner" nitrogen atom in the isocyanogen molecule ($C^{14}NCN$) much lower quadrupolar coupling constant of 1.32 MHz is obtained [26], which is close to that in Sn(NCN). This indicates a high degree of covalent bonding within $^{+}$Sn–N=C=N–Sn^{+} structural motifs in Sn(NCN).

The ^{14}N sideband pattern originates from a single nitrogen environment as shown in a zoomed fragment of the spectrum in Figure 3b, where evenly spaced (by MAS frequency of 7 kHz) spinning sidebands of the Sn(NCN) signal overlap with a sharp resonance of the impurity phase at 270 ppm. There are no spinning sidebands associated with a signal at 270 ppm, hence, this ^{14}N resonance does not exhibit any measurable C_Q even at relatively slow MAS rate of 7 kHz. When compared to the intensity of the entire sideband pattern of the Sn(NCN), it is obvious that the signal integral of the impurity phase at 270 ppm is negligible. We attribute this signal to Sn_3N_4, as its chemical shift and lack of quadrupolar broadening indicates either nitride or oxynitride [30–33]. The appearance of the Sn(NCN) ^{14}N signal that forms a sideband pattern of a single environment indicates that the two nitrogen environments in a $(NCN)^{2-}$ ion are equivalent, otherwise two signals (with distinct chemical shifts) would be expected, and therefore two spinning sidebands patterns formed. The result above renders the ^{14}N solid-state NMR as a powerful method for discrimination of the potential occurrence of cyanamide (N≡C–N^{2-}) or carbodiimide ($^{-}$N=C=N^{-}) moieties in this class of compounds.

To support the interpretation of the experimental data, the ^{13}C isotropic chemical shift and ^{14}N quadrupolar coupling constant of the carbodiimide moiety were calculated with quantum chemistry methods applied to the

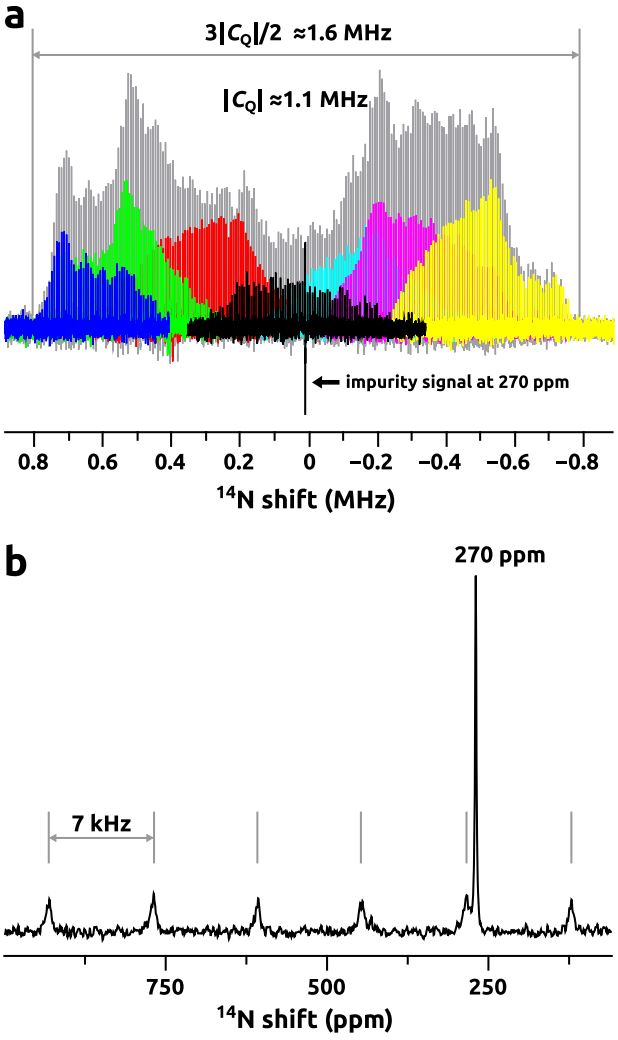

Figure 3: ^{14}N NMR variable-offset DANTE [27–29] spectra of Sn(NCN) (panel a) with the sum of all sub-spectra shown in gray, and ^{14}N spin-echo acquisition of the central fragment of the spectrum around impurity signal at 270 ppm (panel b).

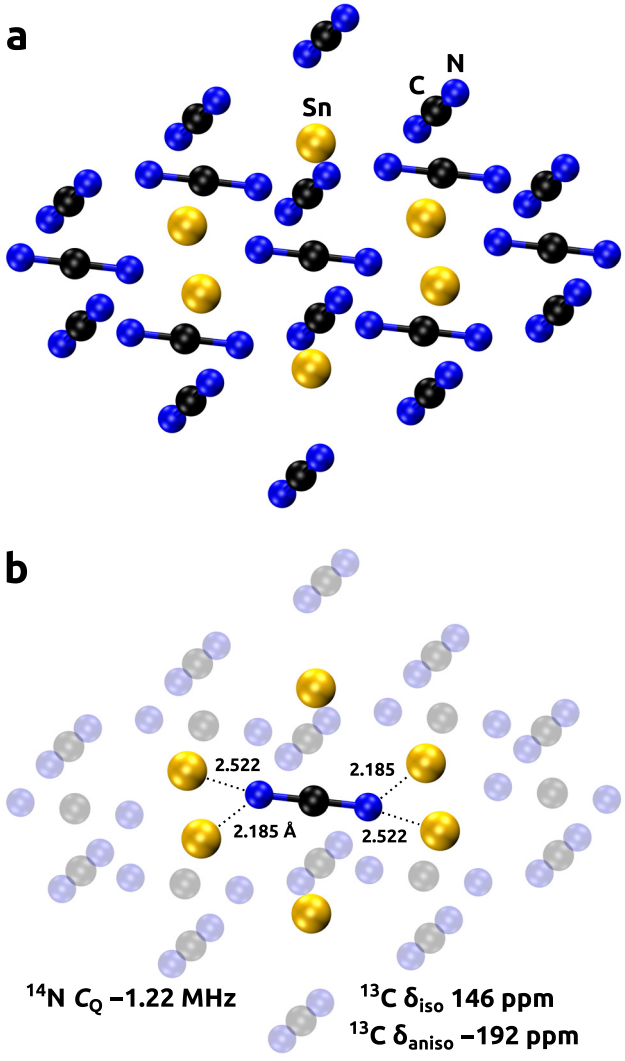

Figure 4: Cluster model of Sn(NCN) used for calculations of NMR properties (panel a) with indicated local environment of the carbodiimide group in the crystal structure (panel b).

cluster model derived from the Sn(NCN) crystal structure. This model consists of six Sn^{2+} ions coordinated by 19 $(NCN)^{2-}$ ions, see Figure 4a.

The calculations of ^{13}C δ_{iso} for the central $^{-}$N=C=N^{-} unit (Figure 4b) involved perturbatively-corrected, "double-hybrid" DFT (with DSD-PBEP86 approximation and MP2 relaxed density), whereas calculations of ^{14}N C_Q were performed with the domain-based local pair natural orbital coupled cluster singlets and doublets (DLPNO-CCSD) method (through the unrelaxed CCSD density and so-called Λ-equations). These methods provide accuracy beyond that of standard DFT approaches for prediction of NMR parameters [33–39]. The core-property pcSseg-2 (for δ_{iso}) and aug-cc-pVTZ-J (for C_Q) basis sets were employed, which were specifically developed for accurate prediction of NMR properties [40, 41]. The ^{13}C NMR shielding tensors were obtained with the GIAO approach [42]. The isotropic ^{13}C NMR shielding $\sigma_{iso} = (\sigma_{xx} + \sigma_{yy} + \sigma_{zz})/3$ was converted into an isotropic NMR chemical shift δ according to $\delta_{iso} = \sigma^{calc}_{iso,ref} - \sigma^{calc}_{iso} + \delta^{exp}_{iso,ref}$ where δ_{iso} and σ_{iso} correspond to the chemical shift and shielding of the atom of interest, whereas $\sigma^{calc}_{iso,ref}$ and $\delta^{exp}_{iso,ref}$ represent the calculated shielding and experimental shift of the reference, respectively. The CO_2 molecule in the gas phase was used as a reference [37]. The molecular geometry of the CO_2 reference was optimized at the CCSD(T)/cc-pVTZ level of theory.

The calculated ^{13}C isotropic chemical shift δ_{iso} = 146 ppm is in excellent agreement with the experimental result of 148 ppm. Moreover, the calculated CSA $\delta_{aniso} \approx -192$ ppm agrees very well with the experimental estimate of ~−200 ppm. In fact, the predicted ^{13}C CSA for the carbodiimide $^{-}N{=}C{=}N^{-}$ ion in the Sn(NCN) crystal structure is very similar to that calculated for the O=C=O molecule in the gas phase: −192 and −226 ppm, respectively. Yet, the principal components of the chemical shift tensor $\{\delta_{xx}, \delta_{yy}, \delta_{zz}\}$ predicted for the $^{-}N{=}C{=}N^{-}$ ion in Sn(NCN) {254, 230, −46} are rather similar to those for CO_2 {238, 238, −101}, however, the ^{13}C CSA tensor in Sn(NCN) is axially asymmetric ($\delta_{xx} \neq \delta_{yy} \neq \delta_{zz}$), whereas that for CO_2 displays axial symmetry.

The calculated ^{14}N quadrupolar coupling constant C_Q = −1.22 MHz for the Sn(NCN) model is in very good agreement with the experimental estimate of $|C_Q| \approx 1.1$ MHz. This indicates that the low C_Q observed for the $^{-}N{=}C{=}N^{-}$ ion in Sn(NCN) does not originate from averaging as a result of the motion/dynamics in the crystal structure, and corroborates that ^{14}N solid-state NMR offers a possibility for clear-cut distinction between the carbodiimide and cyanamide ions in these compounds.

3 Conclusions

In summary, the $^{14}N/^{13}C$ MAS NMR results reveal that in Sn(NCN) the $(NCN)^{2-}$ groups exist exclusively in the form of symmetric carbodiimide $^{-}N{=}C{=}N^{-}$ ions with two equivalent nitrogen sites. The ^{14}N quadrupolar coupling constant $|C_Q| \approx 1.1$ MHz is much lower than those observed in molecular compounds that comprise cyano-type moieties (N≡C−). The ^{119}Sn MAS NMR spectrum indicates the local environments of Sn^{2+} ions in Sn(NCN) to be similar to those in SnO. Although the indirect $^{1}J(^{119}Sn-^{117}Sn)$ spin–spin couplings are observed for both clearly, they are much weaker in the case of Sn(NCN). Excellent agreement between the experimental and calculated $^{14}N/^{13}C$ NMR parameters is obtained. This not only corroborates the reliability of the theoretical methods employed, but indicates also that the structural model of Sn(NCN) is robust since NMR properties are very sensitive to the local molecular geometry. Given the rich structural chemistry of (NCN)-based compounds, our results demonstrate that solid-state NMR spectroscopy is a powerful tool to distinguish the anionic species, *i.e.*, carbodiimide or cyanamide, and could be also potentially applied for studying structural changes upon electrochemical cycling of (NCN)-based electrode materials.

4 Experimental section

Sn(NCN) was synthesized according to our previously reported procedure at low temperatures (623–823 K) by using an urea precursor route. The precursor was produced by dissolving 2 g (5.7 mmol) of tin(IV) chloride pentahydrate ($SnCl_4{\cdot}5H_2O$, >99%, Sigma Aldrich) powder in ethanol, 0.342 g (5.7 mmol) urea (>99%, Sigma Aldrich) was added and the resulting solution dried under vacuum. The precursor was heated under a NH_3 atmosphere at 673–823 K (10 K min^{-1}) for 2 h. The sample was then cooled down to room temperature under argon atmosphere. Since the temperature range for the synthesis of Sn(NCN) and Sn_3N_4 is very narrow, a minor impurity phase of the latter was present in the XRD patterns; similar as to previous reports on Sn(NCN) [15, 18].

An ambient temperature PXRD pattern was collected on a Panalytical X'Pert PRO Alpha-1 diffractometer operated with Cu $K\alpha_1$ radiation. The powder sample was mounted on a Si wafer zero-background holder and diffraction patterns were measured in a 2θ range from 10 to 80°.

The ^{14}N MAS NMR spectra were acquired at the magnetic field B_0 = 14.1 T (43.4 MHz ^{14}N Larmor frequency), whereas those for ^{13}C and ^{119}Sn at B_0 = 9.4 T (100.6 and 149.2 MHz Larmor frequencies for ^{13}C and ^{119}Sn, respectively). Experiments were performed with a Bruker Avance-III spectrometer and the 7 mm MAS probeheads were used with the MAS rate of 7.00 kHz. The ^{13}C and ^{119}Sn spectra were collected with a single-pulse (Bloch decay) protocol with a 90° radiofrequency (rf) excitation pulse of 5 μs at the nutation frequency of 50 kHz. Sixty-four signal transients with a 3600 s relaxation delay were collected for ^{13}C and 2048 scans with a 60 s relaxation delay for ^{119}Sn. In order to increase band width the step-wise ^{14}N acquisitions involved a DANTE sequence [27–29] with a train of short, rotor-synchronized rf pulses operating at the nutation frequency of 36 kHz. About 12,288 scans with 1s relaxation delay were collected per spectrum, and the offset difference between the subsequent acquisitions was ~200 kHz. An additional ^{14}N spin-echo acquisition of the central region of the signal pattern was recorded with a 90/180° rf pulses of 7/14 μs at the same power level as for DANTE. About 65,536 scans with 1 s relaxation delay were accumulated. The ^{13}C, ^{119}Sn, and ^{14}N shifts were referenced with respect to tetramethylsilane (TMS) at 0 ppm, solid SnO at −208 ppm, and solid NH_4Cl at 0 ppm, respectively.

All calculations of NMR parameters were performed with the ORCA code [43, 44] using very tight convergence tolerance of 1×10^{-9} E_h. The evaluation of Coulomb and exchange integrals was accelerated with the RIJCOSX [45] approximation with very tight grid (GridX8) and employing either def2/J Coulomb-fitting basis set [46] or automatic basis set generation procedure [47] (see the Supporting Information for details). The DSD-PBEP86 calculations employed very tight integration grid (Grid7 NoFinalGrid) and no frozen core electrons. The DLPNO-CCSD calculation was performed with a Foster-Boys localization scheme, a full MP2 guess, all electrons on carbon and nitrogen being correlated, and ThightPNO truncation settings employed for the central carbodiimide group and the six Sn atoms, whereas the embedding NCN groups were treated at the Hartree–Fock level of theory.

5 Supporting information

Cartesian coordinates of the cluster model and the CO_2 reference are given as Supporting Information available online (https://doi.org/10.1515/znb-2021-0122).

Author contributions: All the authors have accepted responsibility for the entire content of this submitted manuscript and approved submission.
Research funding: None declared.
Conflict of interest statement: The authors declare no conflicts of interest regarding this article.

References

1. Mallmann M., Häusler J., Cordes N., Schnick W. *Z. Anorg. Allg. Chem.* 2017, *643*, 1956–1961.
2. Sougrati M. T., Arayamparambil J. J., Liu X., Mann M., Slabon A., Stievano L., Dronskowski R. *Dalton Trans*. 2018, *47*, 10827–10832.
3. Corkett A. J., Chen Z., Bogdanovski D., Slabon A., Dronskowski R. *Inorg. Chem.* 2019, *58*, 6467–6473.
4. Chen Z., Löber M., Rokicinska A., Ma Z., Chen J., Kustrowski P., Meyer H. J., Dronskowski R., Slabon A. *Dalton Trans*. 2020, *49*, 3450–3456.
5. Chen Z., Löber M., Corkett A. J., de Bruin-Dickason C., Chen J., Rokicinska A., Kustrowski P., Dronskowski R., Slabon A. *Inorg. Chem.* 2020, *59*, 13589–13597.
6. Krings M., Montana G., Dronskowski R., Wickleder C. *Chem. Mater.* 2011, *23*, 1694–1699.
7. de Rohello E. L., Suffren Y., Merdrignac-Conanec O., Guillou O., Calers C., Cheviré F. *J. Solid State Chem.* 2021, *300*, 122240.
8. Davi M., Drichel A., Mann M., Scholz F., Schrader T., Rokicinska A., Kustrowski P., Dronskowski R., Slabon A. *J. Phys. Chem. C* 2017, *121*, 26265–26274.
9. Davi M., Mann M., Ma Z., Schrader F., Drichel A., Budnyk S., Rokicinska A., Kustrowski P., Dronskowski R., Slabon A. *Langmuir* 2018, *34*, 3845–3852.
10. Fu Z., Wang Y., Li Z., Song T., Long B., Ali A., Deng G. J. *J. Colloid Interface Sci.* 2021, *593*, 152–161.
11. Sougrati M., Darwiche A., Liu X., Mahmoud A., Hermann R. P., Jouren S., Monconduit L., Dronskowski R., Stievano L. *Angew. Chem. Int. Ed.* 2016, *55*, 5090–5095.
12. Sougrati M., Darwiche A., Liu X., Mahmoud A., Hermann R. P., Jouren S., Monconduit L., Dronskowski R., Stievano L. *Angew. Chem.* 2016, *128*, 5174–5179.
13. Li T., Zhao W., Bi H., Tang Y., Huang F. *J. Power Sources* 2020, *467*, 228252.
14. He W., Li H., Long B., Xiao M., Song T., Wang X., Tong Y. *ACS Appl. Energy Mater.* 2021, *55*, 4290–4296.
15. Braun C., Mereacre L., Hua W., Sturzer T., Ponomarev I., Kroll P., Slabon A., Chen Z., Damour Y., Rockquefelte X., Halet J. F., Indris S. *ChemElectroChem* 2020, *7*, 4550–4561.
16. Pecher O., Carretero-Gonzalez J., Griffith K. J., Grey C. P. *Chem. Mater.* 2016, *29*, 213–242.
17. Forse A. C., Griffin J. M., Merlet C., Carretero-Gonzalez J., Raji A. O., Trease N. M., Grey C. P. *Nat. Energy* 2017, *2*, 16216.
18. Löber M., Dolabdjian K., Ströbele M., Romao C. P., Meyer H. *J. Inorg. Chem.* 2019, *58*, 7845–7551.
19. Dolabdjian K., Görne A., Dronskowski R., Ströbele M., Meyer H. *J. Dalton Trans.* 2018, *47*, 13378.
20. Cossement C., Darville J., Gilles J. M., Nagy J. B., Fernandez C., Amoureux J. P. *Magn. Reson. Chem.* 1992, *30*, 263–270.
21. Anet F. A. L., Yavari I. *Org. Magn. Reson.* 1976, *3*, 327–328.
22. Yavari I., Roberts J. D. *J. Org. Chem.* 1978, *43*, 4689–4692.
23. Szewczyk I., Rokicińska A., Michalik M., Jianhong C., Jaworski A., Aleksis R., Pell A. J., Hedin N., Slabon A., Kuśtrowski P. *Chem. Mater.* 2020, *32*, 7263–7273.
24. Chen Z., Jaworski A., Chen J., Budnyak T., Szewczyk I., Rokicińska A., Dronskowski R., Hedin N., Kuśtrowski P., Slabon A. *Dalton Trans*. 2021, *50*, 6857–6866.
25. Murray S. G., Kukolich A. M. *J. Chem. Phys.* 1983, *78*, 3557.
26. Gerry M. C. L., Stroh F., Winnewisser M. *J. Mol. Spectrosc.* 1990, *140*, 147.
27. Vitzthum V., Caporini M. A., Ulzega S., Bodenhausen G. *J. Magn. Reson.* 2011, *43*, 234–239.
28. Vitzthum V., Caporini M. A., Ulzega S., Trébosc J., Lafon O., Amoureux J. P., Bodenhausen G. *J. Magn. Reson.* 2012, *43*, 228–236.
29. Lu X., Trébosc J., Lafon O., Carnevale D., Ulzega S., Bodenhausen G., Amoureux J. P. *J. Magn. Reson.* 2013, *43*, 105–116.
30. Kempgens P., Britton J. *Magn. Reson. Chem.* 2016, *54*, 371–376.
31. Cordes N., Bräuniger T., Schnick W. *Eur. J. Inorg. Chem.* 2018, 5019–5026.
32. Ma Z., Jaworski A., George J., Rokicińska A., Thersleff T., Budnyak T. M., Hautier G., Pell A. J., Dronskowski R., Kuśtrowski P., Slabon A. *J. Phys. Chem. C* 2020, *124*, 152–160.
33. Ma Z., Lu C., Chen J., Rokicińska A., Kuśtrowski R., Coridan P., Dronskowski R., Slabon A., Jaworski A. *Z. Naturforsch*. 2021, *76B*, 275–280.
34. Kozuch S., Martin J. M. L. *Phys. Chem. Chem. Phys.* 2011, *13*, 20104–20107.
35. Stoychev G. L., Auer A. A., Neese F. *J. Chem. Theor. Comput.* 2018, *14*, 4756–4771.
36. Saitow M., Neese F. *J. Chem. Phys.* 2018, *149*, 034104.
37. Rzepka P., Bacsik Z., Pell A. J., Hedin N., Jaworski A. *J. Phys. Chem. C* 2019, *123*, 21497–21503.
38. Witwicki M., Walencik P. K., Jezierska J. *J. Mol. Model.* 2020, *138*, 104113.
39. Dittmer A., Stoychev G. L., Maganas D., Auer A. A., Neese F. *J. Chem. Theor. Comput.* 2020, *16*, 6950–6967.
40. Provasi P. F., Aucar G. A., Sauer S. P. A. *J. Chem. Phys.* 2001, *115*, 614–620.
41. Jensen F. *J. Chem. Theor. Comput.* 2015, *11*, 132–138.
42. Wolinski K., Hilton J. F., Pulay P. *J. Am. Chem. Soc.* 1990, *112*, 8251–8260.
43. Neese F. *Wiley Interdiscipl. Rev. Comput. Mol. Sci.* 2011, *2*, 73–78.
44. Neese F., Wennmohs F., Becker U., Riplinger C. *J. Chem. Phys.* 2020, *152*, 224108.
45. Neese F., Wennmohs F., Hansen A., Becker U. *Chem. Phys.* 2009, *356*, 98–109.
46. Weigend F. *Phys. Chem. Chem. Phys.* 2006, *8*, 1057–1065.
47. Stoychev G. L., Auer A. A., Neese F. *J. Chem. Theor. Comput.* 2017, *13*, 554–562.

Supplementary Material: The online version of this article offers supplementary material (https://doi.org/10.1515/znb-2021-0122).